An ultrabright, narrowband source of polarization-entangled photons

by

Eser Keskiner

Submitted to the Department of Electrical Engineering and Computer Science
in partial fulfillment of the requirements for the degree of

Master of Engineering in Electrical Engineering and Computer Science

at the

MASSACHUSETTS INSTITUTE OF TECHNOLOGY

August 2001

Author.....
Department of Electrical Engineering and Computer Science
August 7, 2001

Certified by.....
Ngai Chuen Wong
Principal Research Scientist, Research Laboratory of Electronics
Thesis Supervisor

Accepted by.....
Arthur C. Smith
Chairman, Department Committee on Graduate Theses

An ultra-bright narrowband source of polarization-entangled photons

by

Eser Keskiner

Submitted to the Department of Electrical Engineering and Computer Science
on August 7, 2001, in partial fulfillment of the
requirements for the degree of
Master of Engineering in Electrical Engineering and Computer Science

Abstract

A type-II phase-matched, doubly-resonant KTP optical parametric amplifier (OPA) was pumped at 532 nm near frequency degeneracy to produce a high-flux source of entangled photons with an inferred production rate of 1.8 x 10^6 pairs/sec at 100 μW of pump power. The output consisted of three distinct components: narrowband doubly-resonant pairs, narrowband singly-resonant pairs and broadband nonresonant pairs. The broadband nonresonant pairs comprised polarization triplet states under frequency degeneracy. Quantum interference between the OPA output pairs has been observed for the triplet states that were analyzed with a polarizer set at 45° relative to the output polarizations of the OPA.

Thesis Supervisor: Ngai Chuen Wong
Title: Principal Research Scientist, Research Laboratory of Electronics

Acknowledgements

First and foremost, I would like to thank Dr. Franco Wong for giving me the opportunity to work on this project and for his invaluable support and help during all the stages of the work presented in this thesis, as well as during the writing of my thesis. It has been a great privilege learning from him during the past one and a half years.

I would also like to thank Professor Jeffrey Shapiro for all the insights he has provided in the analysis of the data, and being available for productive discussions.

I have learned tremendously from all the members of the Quantum Communications MURI Group and I would like to express my gratitude to all of them. The group meetings we have had helped me keep a broader perspective on the implications of our research when it was too easy to get lost in small experimental details.

It has been a great experience working with all the members of our group. I would like to thank Chris Kuklewicz from whom I have learned so much during the course of the project. I am grateful to Marius Albota for always being there to help me out during the hard times of which there were many. Elliott Mason has been an invaluable resource on several topics and I have benefited tremendously from his experience in optics. I would also like to thank Emily Nelson for the thorough theoretical work she has done on the experiments. Her thesis has been an invaluable resource for me.

Throughout my five years at MIT, I was fortunate to have many great friends around me who have helped me in many ways and made life more enjoyable. My special thanks to Cemal, Nicole and Wojciech for always being there for me. I would also like to thank my best friends from high school, Salahi, Tufan, Emre and Orhan. They have been a constant source of support over the past five years.

Last, but not least, I would like to thank my family for all their love and support. My parents have allowed me the freedom to grow into the person I am and have always supported me in all the decisions I have made. Their confidence in me has always kept me going long after I thought I could not. I am forever indebted to them. My brother (and first teacher) Yener not only taught me how to read and write, but also paved the way to my accomplishments through primary and secondary education. I would not be where I am today had it not been for him.

Contents

List of Figures

Chapter 1

Introduction

In recent years, the concept of quantum entanglement has played an increasingly important role in the field of quantum information processing. Theoretical and experimental progress in this field, as well as the discovery of novel non-classical features in multi-particle situations have led to increased interest in various applications of entangled states such as quantum communication [1], quantum cryptography [2], quantum teleportation [3] and quantum computing.

An MIT and Northwestern University (MIT/NU) team has recently proposed a singlet-based quantum communication protocol for long-distance quantum teleportation [4]. In this scheme, polarization-entangled photon pairs are generated and one photon of each pair is sent to the transmitter station Alice and the other photon of the pair is sent to the receiver station Bob. The polarization-entangled photons are then loaded into trapped-atom quantum memories [5] at Alice and Bob for storage that can be retrieved later. The polarization-entangled photons do not carry any information but are used to prepare Alice and Bob with stored polarization entanglement that can be used for quantum teleportation of the polarization state of a photon. Also, the stored polarization-entangled quantum bits (qubits) can be utilized to create a one-time secret key pad for encryption.

The main focus of this thesis is the investigation of the feasibility of an ultrabright narrowband source for polarization-entangled photons. In this chapter, I present the

previous work done in the field and the MIT/NU scheme for quantum communication. I detail the experimental apparatus and setup in Chapter 2. In Chapter 3, I present the results and analysis of the experiment and in Chapter 4 some concluding remarks are presented.

1.1 Previous Work

The standard method for generating polarization entanglement is by optical spontaneous parametric downconversion. This nonlinear process involves the generation of two daughter photons (called signal and idler) in a nonlinear optical crystal by absorbing a pump photon that is at a higher frequency. Energy is conserved in the process and the pump (ω_P), signal (ω_S) and idler (ω_I) frequencies are related by $\omega_P = \omega_S + \omega_I$. Efficient parametric downconversion occurs if there is momentum conservation that leads to the phase matching condition of the nonlinear crystal at the operating wavelengths.

Using type-II phase matching, orthogonally polarized signal and idler photons are generated. They are emitted into two cones, one being polarized along the ordinary axis of the crystal, and the other along the extraordinary axis. The angular separation of the two cones depends on the phase matching condition, the angle between the pump beam and the optic axis of the crystal, and also the divergence of the pump beam. Assuming degenerate operation with $\omega_I \approx \omega_S$, in the areas where the two cones overlap, the light can be described in the polarization entangled state

$$|\psi\rangle = \frac{(|H_1V_2\rangle + e^{i\alpha}|V_1H_2\rangle)}{\sqrt{2}},$$

where H and V represent horizontal and vertical polarizations and α is the relative phase shift of the signal and idler due to the birefringence of the crystal. Using a half-wave

plate in one path, the four EPR-Bell states, which form a maximally-entangled basis, can be obtained. These bases are

$$|\psi^{\pm}\rangle = \frac{|H_1V_2\rangle \pm |V_1H_2\rangle}{\sqrt{2}},$$

$$|\varphi^{\pm}\rangle = \frac{|H_1H_2\rangle \pm |V_1V_2\rangle}{\sqrt{2}}.$$

By using parametric downconversion from a type-II phase-matched beta barium borate (BBO) crystal, Kwiat *et al* [6] have demonstrated the generation of up to ~2000 polarization entangled photon pairs per second for a pump power of 150 mW. However, this source has the disadvantage of having a limited brightness since entanglement is observed only along two special directions.

More recently Kwiat and coworkers have developed a much brighter source in which two identical, thin crystals were used [7]. The two type-I phase-matched BBO crystals were placed adjacent to one another, and they were oriented with their optic axes at 90° with respect to each other. All pairs of a given wavelength generated by this source are entangled. Figure 1-1 shows the experimental setup of this experiment.

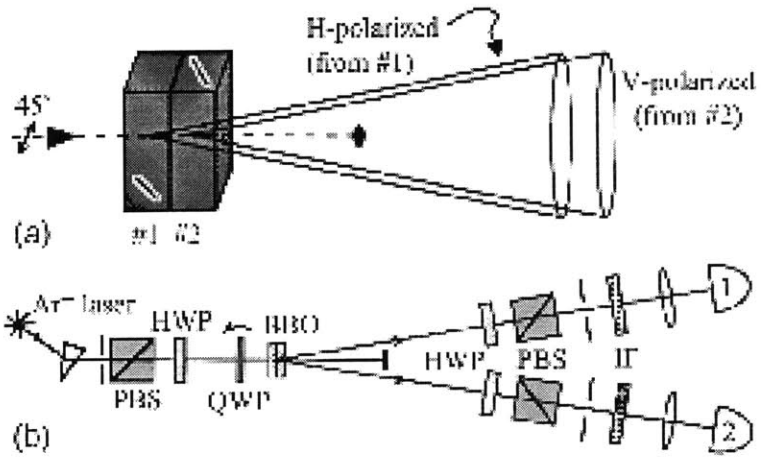

Figure 1-1: Experimental setup of ultrabright source of polarization entangled Photons, from [7].

In this setup, the optic axis of one of the BBO crystals defines the horizontal plane and the optic axis of the other defines the vertical plane. Due to type-I phase matching, for a vertically polarized pump beam, downconversion occurs only in crystal 1, where the pump is extraordinary polarized resulting in light cones that are horizontally polarized. For a horizontally polarized pump beam, downconversion only occurs in crystal 2, and the light cones that are generated are vertically polarized. Except for the different polarizations, the cones are identical. When the pump beam is polarized at 45°, each photon from the pump is equally likely to be downconverted in either crystal. Thus the outputs from the setup are randomly polarized and indistinguishable, which are characteristic of polarization entanglement.

Using this experimental setup, Kwiat *et al* have demonstrated the generation of polarization-entangled photons at a rate of 1.5×10^6 pairs per second over a 5 nm bandwidth at a 702-nm center wavelength and with 150 mW pump power. Although this source is ten times brighter than any previously reported source, its broadband nature is

not suitable for narrowband applications. In particular, in the MIT/NU-proposed protocol, the trapped-atom quantum memory is most efficiently loaded with entangled photons that have a spectral bandwidth of ~30 MHz which means that the source described in [7] would be spectrally too weak for such applications.

The "quantum memory" model described in [5] proposes to use trapped Rubidium (Rb) atoms in high-finesse cavities as quantum memory nodes. Two Rb atoms, each absorbing one of the entangled photon pair, share the quantum entanglement and can act as the "transmitter" and "receiver" terminals of a quantum communication channel. The capture and storage of entanglement is affected by several factors including transmission losses and absorption efficiency of the cavities. The trapped Rb atoms suggested for storing the photonic entanglement have a wavelength of 795-nm and at this wavelength, the source developed by Kwiat *et al* has a pair generation rate of only 15/s within a 30-MHz bandwidth. Clearly this broadband source is not suitable for the MIT/NU scheme, especially when propagation losses are inevitable in long-distance quantum teleportation.

Recently Shapiro and Wong [8] proposed a scheme for generating a high-flux, narrowband source of polarization-entangled photon pairs that can be 5 orders of magnitude higher in spectral brightness when compared to the Kwiat source [7]. Like the two experiments described in [6, 7], the source of polarization entangled photons envisioned by Shapiro and Wong uses second order nonlinear optical interactions. However, the source described in [8] uses cavity-enhanced parametric amplification instead of spontaneous parametric downconversion used in the other sources.

Parametric amplification and parametric downconversion differ in the spectral properties of the daughter photons generated from the $\chi^{(2)}$ interactions. If the crystal used

for optical parametric downconversion is placed inside an optical resonator, the signal and idler fields can build up to large values. The signal and idler cavities formed within such a resonator can generate enough positive feedback to cause oscillations. This process is known as optical parametric oscillation. If the cavity is pumped at a power below the threshold level at which oscillations start, we get optical parametric amplification. An optical parametric amplifier (OPA) is schematically represented in Figure 1-2. Because of the cavity, the resonant signal and idler fields within the cavity bandwidth are significantly higher than the nonresonant fields of a parametric downconverter for a given pump power, leading to lower required pump powers and narrower spectral width for the entangled photons. By varying the crystal's phase matching parameter and the cavity resonance peak, the OPA can be frequency tuned.

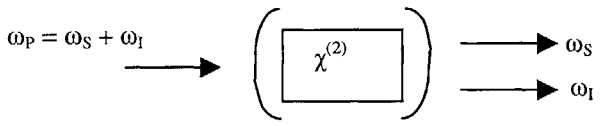

Figure 1-2: Optical Parametric Amplifier. ω_P is the pump frequency, ω_I is the idler frequency and ω_S is the signal frequency.

The setup described in [8] uses two doubly resonant (in which both the signal and the idler fields are in resonance) type-II phase-matched OPAs that are pumped at equal power and phase.

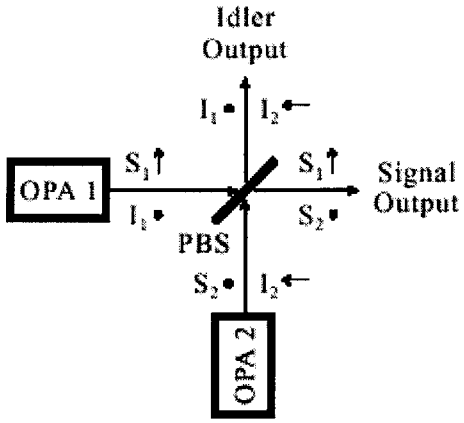

Figure 1-3: Dual OPA Configuration. S_1 (S_2) and I_1 (I_2) are the signal and idler from OPA 1 (2).

Figure 1-3 shows the dual-OPA configuration. The signal and idler fields from each OPA are orthogonally polarized due to type-II phase matching. The two amplifiers are assumed to be pumped at the same power with identical crystal and cavity parameters. The polarizing beamsplitter (PBS) passes photons with a polarization parallel to the plane of incidence (p-polarized) and reflects those that are perpendicular to the plane of incidence (s-polarized). This arrangement of combining signal and idler photons from the two amplifiers works regardless of whether the amplifiers are operated at frequency degeneracy or not.

For ideal doubly resonant OPAs with no excess pump noise, no pump depletion, zero detuning, no cavity loss except at the output coupler and equal linewidths for the signal and the idler, the equations of motion for each OPA are given by [8]

$$\left(\frac{d}{dt}+\Gamma\right)\hat{a}_S(t)=G\Gamma\hat{a}_I^{+}(t)+\sqrt{2\Gamma}\hat{A}_S^{IN}(t), \tag{1.1}$$

$$\left(\frac{d}{dt}+\Gamma\right)\hat{a}_I(t)=G\Gamma\hat{a}_S(t)+\sqrt{2\Gamma}A_I^{IN}(t), \tag{1.2}$$

where Γ is the cavity loss rate, $\hat{a}_S(t)$ and $\hat{a}_I(t)$ are the intracavity annihilation operators for signal and idler, G is the normalized OPA gain, defined by

$$G = \sqrt{\frac{P_p}{P_T}}\ , \tag{1.3}$$

with P_p representing the pump power and P_T representing the oscillation threshold pump power. The signal and idler fields are related to the internal and external input fields by

$$\hat{A}_S(t) = \sqrt{2\Gamma}\hat{a}_S(t) - \hat{A}_S^{IN}(t)\,, \tag{1.4}$$

and

$$\hat{A}_I(t) = \sqrt{2\Gamma}\hat{a}_I(t) - A_I^{IN}(t)\,. \tag{1.5}$$

From the equations above, it can be seen that each OPA produces signal and idler photons that are in a zero-mean pure Gaussian state. Assuming unity quantum efficiency, the number of signal and idler photons counted over a time interval of $0 \le t \le T$ are given by

$$\hat{N}_s \equiv \int_0^T \hat{A}_s^+(t)\hat{A}_s(t)dt\,, \tag{1.6}$$

and

$$\hat{N}_I \equiv \int_0^T \hat{A}_I^+(t)\hat{A}_I(t)dt\,. \tag{1.7}$$

Using the correlation expression

$$< \hat{A}_s^+(t+\tau)\hat{A}_s(t) > = < \hat{A}_I^+(t+\tau)\hat{A}_I(t) >$$

$$= \frac{G\Gamma}{2}\left[\frac{\exp[-(1-G)\Gamma\,|\,\tau\,|]}{1-G} - \frac{\exp[-(1+G)\Gamma\,|\,\tau\,|]}{1+G}\right]\,, \tag{1.8}$$

one can see that the mean number of signal and idler photons in a time interval T is given by

$$\langle \hat{N}_s \rangle = \langle \hat{N}_I \rangle = \frac{G^2 \Gamma T}{1 - G^2}. \qquad (1.9)$$

Therefore, the photon-count difference, $\Delta \hat{N} \equiv \hat{N}_s - \hat{N}_I$ is zero mean. The variance is given by

$$\frac{\langle \Delta \hat{N}^2 \rangle}{\langle \hat{N}_S \rangle + \langle \hat{N}_I \rangle} = \frac{1 - \exp(-2\Gamma T)}{1 - G^2}. \qquad (1.10)$$

This expression approaches 1 for $\Gamma T << 1$ and 0 for $\Gamma T >> 1$. For a time interval T that is much greater than the cavity lifetime $1/\Gamma$, the variance in the photon-counting difference goes to zero, meaning every signal photon in a given polarization is accompanied by an idler photon in the orthogonal polarization. In order not to have more than one pair of entangled photons in a given interval (such that two photons detected within a given time interval can be identified with high confidence as photons from the same pair), the cavity has to be pumped at low power, at about 1% of threshold, or G^2=0.01. Consider the case of a measurement time interval T of 70 ns, and a cavity lifetime of 7 ns (with a corresponding spectral bandwidth of 30 MHz). For low threshold operations, the photon counting measurements are approximately Poissonian, and Shapiro and Wong estimate the conditional probability of detecting the signal (idler) photon given that its idler (signal) partner has been detected as 0.95 [8]. For a coincidence interval T of 70 ns, at 1% threshold operation, the pair generation rate is $G^2\Gamma \approx 1.5 \times 10^6$ sec^{-1}.

This dual-OPA source has the advantage of generating photon pairs in well-defined spatial modes, thus making the collection efficiency much higher. In addition, the cavity linewidth can be easily adjusted by changing the cavity length or the output coupling,

which allows the generation rate to be varied. The realization of this source and the generation of narrowband, high-flux source at 795 nm would make the loading of remote quantum memory nodes more practical.

The focus of this thesis is to investigate the characteristics of an OPA source at the wavelength of 1064 nm. The operating wavelength of 1064 nm instead of 795 nm is chosen because of the immediate availability of a doubly resonant OPA cavity at the 1064-nm wavelength. The results of a dual-OPA source at 1064 nm should be equally applicable at the desired wavelength of 795 nm.

The cavity used in our experiment was well-characterized in a twin-beam generation experiment described in [9]. In that experiment a pump at 531 nm was used and an intensity correlation of 5.5 dB below the shot-noise level was observed. A major disadvantage of operating at this wavelength for entanglement measurements is that the Si photon counting efficiency is low (~1%). Although the detectors we used had significantly lower quantum efficiencies at 1064 nm, the availability of a well-characterized OPA at 1064 nm allowed us to quickly test the proposed scheme of Shapiro and Wong in a proof-of-principle experiment. The theory of using optical parametric amplification to generate entangled photon pairs described in [8] is not wavelength specific. Hence, the generation rate and other properties suggested by Shapiro and Wong could be tested using this cavity although the generated photons would not be at the desired wavelength for quantum storage purposes.

Chapter 2

Experimental Apparatus and Setup

2.1 Experimental Apparatus

2.1.1 Standing Wave Doubly-Resonant OPA

The nonlinear optical system in this experiment was a doubly-resonant optical parametric amplifier (OPA) in a two-mirror standing-wave cavity configuration. This OPA cavity was previously used as an above-threshold triply-resonant optical parametric oscillator (OPO) system that demonstrated ~5.5 dB of nonclassical intensity correlation below the shot noise level [9]. As a result the OPA cavity had been well characterized in this twin-beam generation experiment.

Figure 2-1 shows a schematic of the OPA cavity. The cavity was formed with a 20-cm-radius input mirror M1 coated for maximum reflection at 1064 nm and maximum

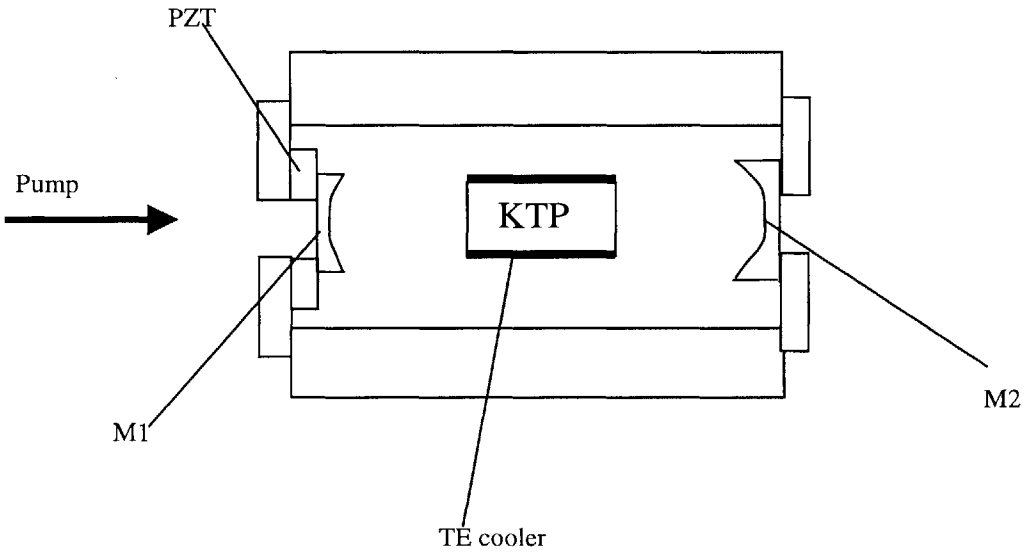

Figure 2-1: Schematic of standing-wave OPA cavity. M1 and M2 are cavity mirrors.

transmission at 532 nm, and a 2-cm-radius output mirror M2 coated for 2.7% transmission at 1064 nm and maximum reflection at 532 nm. Hence the cavity was designed to resonate the subharmonic signal and idler fields at 1064 nm in a double-pass pump configuration. The roundtrip power losses were previously reported to be 0.46% for the extraordinary polarization and 0.66% for the ordinary polarization [9] and the output coupling was reported as 2.69%. The threshold was found to be ~300 mW. The 3 x 3 x 10 mm hydrothermally grown potassium titanyl phosphate (KTP) crystal was antireflection coated at both wavelengths to minimize intracavity losses and it was mounted on a thermo-electric (TE) cooler. The mirrors were separated by 1.9 cm and M1 was mounted on a piezoelectric transducer (PZT) for scanning the cavity length. The TE cooler was used for fine temperature tuning for the KTP crystal, and was mounted on a rotation stage to allow a change of the crystal's phase-matching angle. The three tuning elements (crystal angle, TE cooler, and PZT) permitted the KTP phase matching to be tuned to near frequency degeneracy for the pump wavelength of 532 nm.

In the experiment, we first optimized the cavity alignment by maximizing the second-harmonic generation (SHG) of 532 nm, pumped with a Lightwave 122 diode-pumped Nd:YAG laser at 1064 nm. Since the KTP crystal was type II phase matched, the input polarization of the 1064 nm beam was set at 45° relative to the crystal's *c* axis, which in turn was aligned vertically with respect to the propagation axis. Initially the cavity length was scanned using the PZT to show the transmission peaks for both the vertically and horizontally polarized input beams. The cavity mirrors were not attached to any spring-loaded mirror mounts in order to obtain the best mechanical stability for the cavity. We aligned the input laser beam relative to the cavity and obtained a cavity

finesse of ~190, as expected from an average total roundtrip loss of ~ 3.3%. For SHG, the two transmission peaks were brought together by tuning the crystal's temperature with the TE cooler. We maximized the generated green light by adjusting the crystal's angle to tune the phase matching conditions of KTP. For SHG of 532-nm light the phase matching angle (for the propagation axis) was ~23° relative to the x axis in the x-y plane. The free spectral range of the cavity was 5.6 GHz, which yielded a double-Lorenztian bandwidth of 20 MHz for the output entangled photons. A photograph of the compact OPA cavity is shown in Figure 2-2.

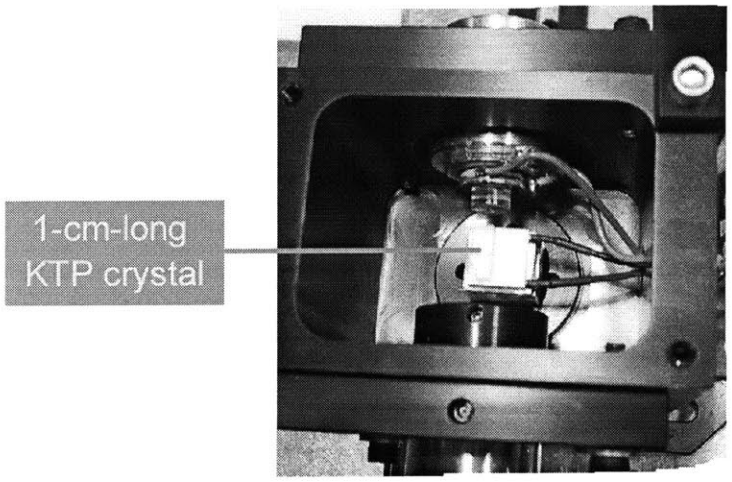

Figure 2-2: Picture of standing wave OPA cavity.

2.1.2 Pump System

The pump source for the experiment was derived from a Coherent Verdi-8 diode-pumped, frequency-doubled Nd:YVO_4 laser with an output power of 8W. The Verdi V-8 laser generated a 532 nm output from the doubling of 1064 nm using a type I phase matched lithium triborate (LBO) crystal. Although the optics within the laser head were coated to transmit 532 nm, some leakage of 1064 nm occured, and precautions had to be taken to make sure none of the radiation at that wavelength reached the detectors.

2.1.3 Detection System

The detection of photons generated in the experiment was performed using Si single photon counting modules (Perkin Elmer Optoelectronics model SPCM-AQR-14). These are modules that can detect single photons of light over the wavelength range from 400 nm to 1060 nm. They can count up to 10^7 events per second with a dead time of 40 ns between events. Each "trigger" event at the detector is converted to a TTL pulse that is 2.5 V high and 25 ns wide in a 50 Ω load. The modules have a dark-count rating of 50-100 counts per second and a detection efficiency of between 1% and 70% depending on the wavelength.

The SPCM-AQR-14 modules are silicon avalanche photodiodes (APDs). They have a "dark count" associated with them, which is defined as the number of pulses one obtains when there is no incident radiation. When the APD is operated in the linear mode, the dark counts are large and it is called the dark current. This dark count is mostly due to thermal effects. When a photon hits the detector biased in the Geiger mode (the mode of operation where the photodiode is operated above its breakdown voltage), it causes an "avalanche" transition of electrons between energy bands. The electron then relaxes to its original position, resulting in a photocurrent that registers as a pulse. However, electrons can be excited to higher energy levels even when there is no incident photon. Thermal effects may cause some electrons to be excited to higher energy levels and then relaxing, leading to a current which also registers as a pulse. These dark-count pulses appear randomly and cannot be distinguished from actual photon counting events due to incident light.

The modules used in our experiments had a maximum dark count rating of 100 counts/s. In order to measure the dark count rate, the modules were shielded with a sheath made with black cardboard, as shown in Figure 2-3 and data was acquired in the dark with no room light.

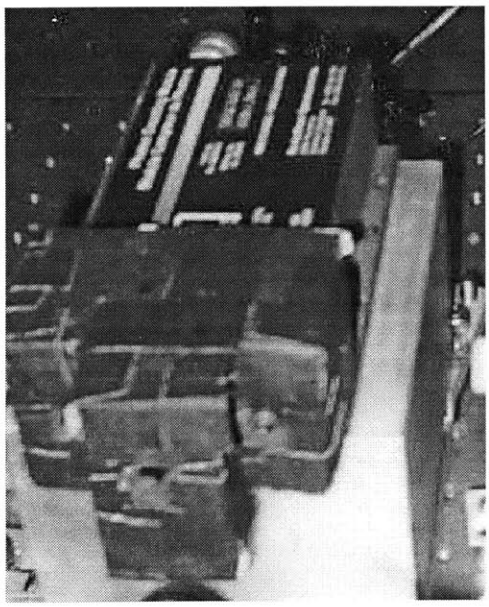

Figure 2-3: Picture of a shielded Single Photon Counting Module.

Table 1 summarizes the results of the dark count tests for the two SPCMs that were used in our experiment. The measurements were made with 100 traces of 20 ms each for each detector. The variance was found to be of the order of the average number of dark counts, indicating these dark counts could be modeled as a Poisson process.

SPCM serial number	Average number of dark counts
5198	47.5 / s
5352	36.5 / s

Table 1: Single photon counting module dark counts.

After verifying that the photon counters had a dark count rate that was well within the given specifications, we set up an experiment to determine their quantum efficiencies. The quantum efficiency of an optical detector is defined as the ratio of the number of detected photons to the number of incident photons and is wavelength dependent. Figure 2-4 shows the experimental setup we used to make a rough estimate of the quantum efficiency of the single-photon detectors (SPD) at 1064 nm, which is the wavelength of the OPA signal and idler outputs.

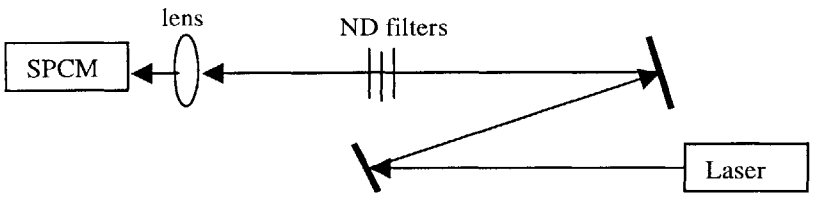

Figure 2-4: Quantum Efficiency Measurement Setup.

An Amoco diode-pumped YAG laser at 1064 nm with a beam waist of 135.5 μm was focused to a waist of 10 μm at the SPD with a f = 15 cm lens. The photon counters had a detector size of 170-μm in diameter. The tight focus, with a corresponding confocal parameter ($b = 2\pi w^2/\lambda$) of 0.59 mm, made it relatively easy to align the beam in the plane perpendicular to the propagation axis. However, the short confocal parameter required careful positioning of the SPD relative to the focusing lens. To enable better spatial control of the location of the focus on the detector, the lens was placed on a three-axis translation stage.

In order to determine the quantum efficiency, the power incident on the photon counting module had to be precisely known. The power from the laser was measured using an optical power meter (Newport Corporation, Model 835) with a sensitivity of 1

nW and a maximum power of 2 mW. It was then attenuated with calibrated neutral density (ND) filters to a level that did not saturate the SPD, or ~ 0.1–1.0 pW. This required an attenuation of several orders of magnitude. A cascade of three to four ND filters was placed in the beam path to accomplish this. For different power levels and different runs of the experiment, quantum efficiencies of between 1.2% and 2% were observed.

The outputs from the two SPDs were sent to two high-speed PC-based digitizing data acquisition boards (Gage Scope's CompuScope model 8500). The associated software from Gage Scope (Version 2.22) was used to control the data acquisition boards. This software package allows multiple boards to operate together to perform simultaneous data acquisition on up to 16 channels at rates up to 125 MHz or on 8 channels at up to 250 MHz. Data analysis was performed using National Instruments LabView, which is a computer-based measurement and automation package.

For fast data acquisition, with a sampling rate of up to 500 MHz, two CompuScope 8500 Cards and GageScope software (Version 2.22) were used. The single-channel analysis of the trigger event due to an incident photon on a single photon detecting module has a typical profile shown in Figure 2-5.

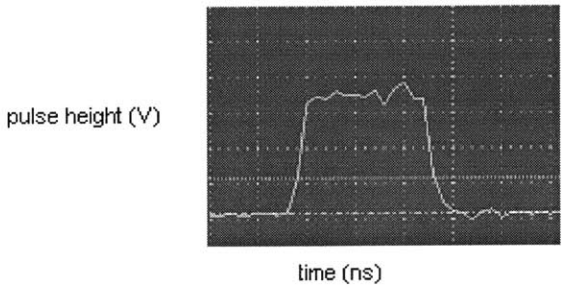

Figure 2-5: Time trace of a detected single photon event. The vertical scale is from –1V to 6V and the horizontal scale covers ~70 ns.

The profile in Figure 2-5 shows that for each detected photon the SPD produced a 30-ns output pulse with a pulse height registering at ~ 3V on the GageScope and a rise time of ~ 5 ns. We decided that in our experiment we would use a sampling rate of 100 MHz that would be fast enough to capture all triggered events but allow us to have data acquisition periods of 20 ms, limited by the on-board memory size of 2 MB. A sample 20-ms GageScope record of one channel is shown in Figure 2-6.

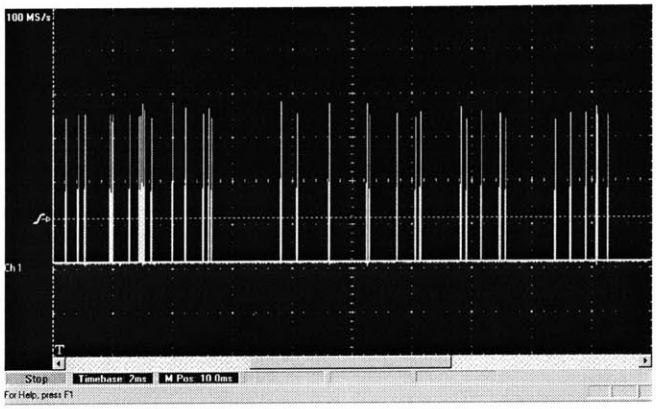

Figure 2-6: Sample single channel record for 20 ms. The vertical scale is from –2V to 6V.

2.2 Experimental Setup

The overall experimental setup is shown in Figure 2-7. Immediately after the Verdi V-8 laser, a Faraday isolator was placed to protect the laser from being damaged by backreflections. The laser beam was then collimated using a collimating lens. For our purposes, a constant beam size over a distance of 4-5 meters was considered to be adequate since the whole path of the beam from the laser to the OPA was less than half of that distance. A half-wave plate was placed after the collimating lens to control the power from the laser that reached the OPA. A polarizer was used after the collimating lens to

bring the laser beam to the desired polarization. In this thesis, "horizontal" polarization refers to polarization that is parallel to the surface of the optical bench and "vertical" polarization refers to polarization that is vertical to the surface of the bench. The polarizer was set at an angle to pass only horizontally polarized light of the pump.

As mentioned in Section 2.1.2, the Verdi V-8 laser generated 532 nm by doubling the 1064 nm light. Some preliminary calculations showed that there might be as much as 1 μW of 1064 nm leakage from the laser. This would correspond to a significant number of photons at the wavelength of interest that could be mistaken for downconverted photons. Hence, a series of three infrared blocking filters (Andover Corporation BG-39, 039FG11-50) were used, each of which had a transmission of 96% for 532 nm and a transmission of less than 0.001% for 1064 nm. After these filters, the number of photons at 1064 nm that could make it to the cavity was essentially down to zero.

Two lenses of focal length 5.7 cm and 1 m were used for modematching the pump into the cavity. They were antireflection-coated for 532 nm. A Gaussian beam of radius w and radius of curvature R can be represented by [10]

$$\frac{1}{q}=\frac{1}{R}-j\frac{\lambda}{\pi w^2}\ . \tag{2.1}$$

It is possible to use $ABCD$ matrix multiplication to solve for a stable q-parameter inside the cavity [11],

$$q=\frac{A-D}{2C}+\sqrt{\left(\frac{A+D}{2C}\right)^2-\frac{1}{C^2}} \tag{2.2}$$

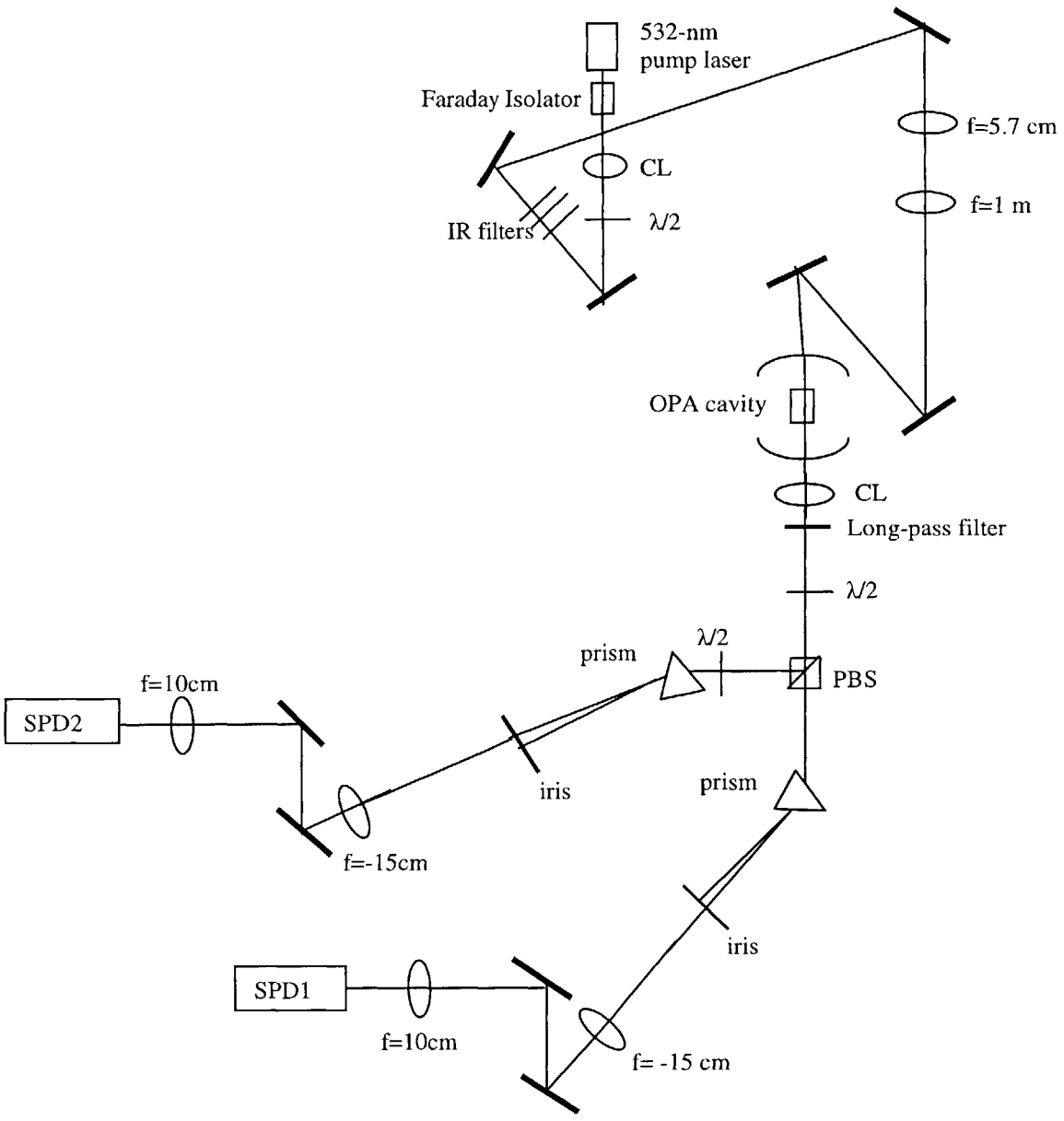

Figure 2-7: Overall experimental setup. CL, collimating lens; λ/2, half-wave plate; PBS, polarizing beamsplitter; SPD, single photon detector.

where *A, B, C* and *D* are elements representing a round-trip through the cavity. Once the *q* parameter at the input mirror was known, the focal lengths and the locations of the two modematching lenses could be determined to modematch the pump into the cavity.

These calculations gave a minimum beam radius w_o of 39.33 μm at 0.104 cm from the output mirror of radius R = 200 mm. After the cavity, a lens of focal length 15 cm was placed, followed by a long-pass filter with a high attenuation for 532 nm to get rid of a significant portion of the pump power leaking through the cavity. The filter used was almost transparent for 1064 nm. Extreme care had to be taken to make sure no pump power reached the detectors, since they had a significantly higher quantum efficiency at the pump wavelength and even a small amount of pump power could distort the number of counted photons.

After the long-pass filter, a half-wave plate was placed in the beam path. The half-wave plate was followed by a polarizing beam splitter, which would reflect vertically polarized radiation and transmit horizontally polarized light. As mentioned before, it was critical to eliminate possible leakage of 532-nm photons from the pump into the detectors. Hence, fused silica prisms were placed in both the reflected and the transmitted beam paths to separate the 1064 nm radiation from the 532-nm pump radiation. The prisms were positioned such that the beam was incident at Brewster's angle for 1064 nm. A half-wave plate was placed in the reflected path to rotate the polarization of the photons by 90° to take advantage of lossless transmission at Brewster's angle, which holds only for TM polarization.

The lens, which was placed after the cavity, focused light at the two wavelengths to their respective foci at a distance 31 cm from the prism. At that point, the spatial separation between the output beam and the pump beam was 6.4 mm and the beam radii were approximately 75 μm and 55 μm, and the maximum ratio of beam separation to beam size was obtained. Irises were placed on both the transmitted and the reflected paths

at that location and the position and size of the irises were set to pass all the photons at 1064 nm but block those at 532 nm. All the components in both paths starting with the irises were enclosed in another dark box as shown in Figure 2-8 to minimize the possibility of stray radiation being detected at the single photon detectors, SPD1 and SPD2. The detectors were shielded with an internal sheath as can be seen in Figure 2-3. With the box and the sheath on, and with measurements taken with all the lights off, the number of background counts was essentially down to the dark count level of the detectors.

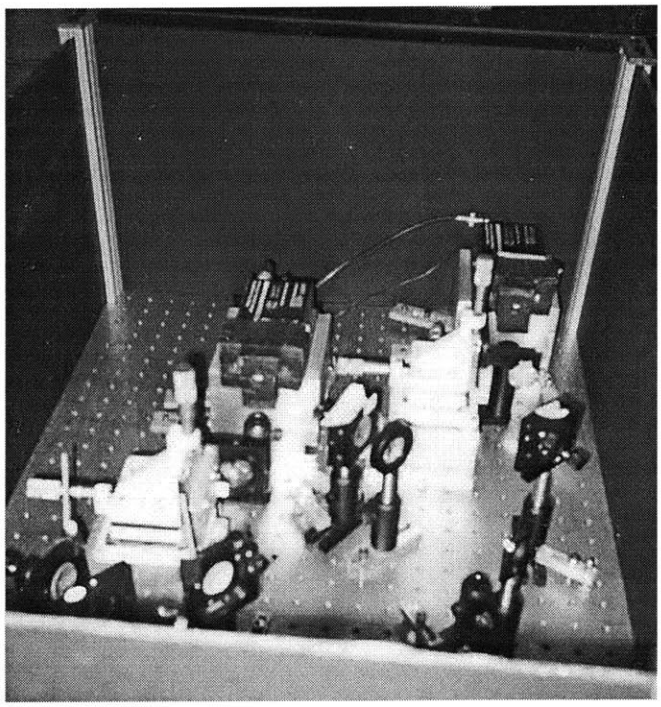

Figure 2-8 External Shielding of the detection unit.

After the irises, the beams had to be focused on the detectors. In order to shorten the distance between the irises and the detectors, we used negative lenses to expand the beam before focusing it onto the detectors. We used a pair of folding mirrors in each path to enable beam steering. A focusing lens of focal length 10 cm was used in each path to focus the beam onto the respective detector. As in the quantum efficiency measurements

described in Section 2.1.3, the lenses were placed on three-axis translation stages to allow for better controls of the location of the focus. The beam radii on the detectors were estimated to be 40 μm.

The losses associated with the optics from the beamsplitter to the detectors were measured to be between 5% and 10% and these losses were within 1% of each other for the transmitted and reflected paths for a given angle at the analyzer half wave plate.

Chapter 3

Experimental Results and Analysis

In this chapter, we present the experimental details including the data acquisition procedure, followed by the results and data analysis. The purpose of the experiment was to investigate the characteristics of an OPA source at the wavelength of 1064 nm. Through the use of a cavity, signal and idler fields are generated within a narrow frequency band. The theory developed in [8] derives the singles and pairs generation rates for an OPA source such as the one we used for our experiment. The expressions for singles rates and pairs rates for sample values of coincidence interval, cavity lifetime and threshold were presented in Chapter 1. To experimentally test these values, the coincidence-measurement setup schematically shown in Figure 3-1 was used.

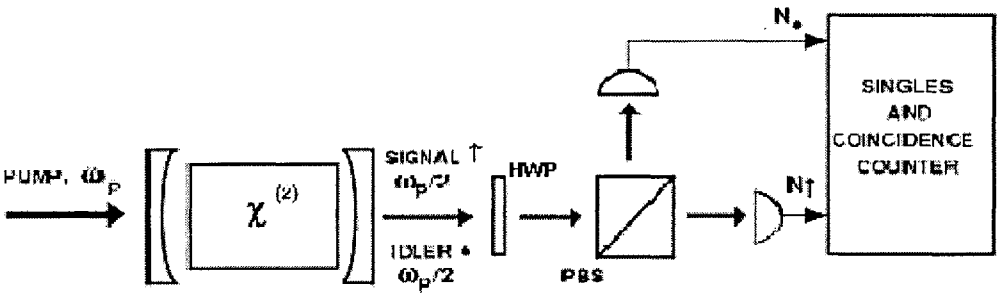

Figure 3-1 Schematic of the coincidence counting setup. The half-wave plate (HWP) and the polarizing beam-splitter (PBS) are used to analyze the singles rates and coincidences for different cases of interest.

The coincidence-counting measurement worked as follows: The signal and idler photons leaving the cavity were orthogonally polarized due to type-II phase matching. By varying the angle of the half-wave plate (HWP), different sets of data were acquired to

investigate the presence of the expected quantum interference effects. The half-wave plate introduced a relative phase difference of 180° between polarizations aligned with its fast and slow axes, effectively rotating the input polarization by a fixed amount. The polarizing beamsplitter transmitted horizontally polarized light and reflected vertically polarized light and it served as a polarization analyzer.

For the experiment, the pump power had to be adjusted such that the pair generation rate was low enough to ensure not more than one pair of photons was generated within a few cavity lifetimes. The cavity lifetime was related to the loss rate of the cavity and determined how long, on average, a photon remained in the cavity before finally leaking out. Pumping the cavity at high power levels would result in the generation of many pairs within a cavity lifetime, and could result in accidental coincidences due to photons that were not generated simultaneously, but detected within the same measurement time interval T. Correlations exist only between the photons of a pair that are generated by the same pump photon and the inclusion of coincidence counts for non-simultaneously generated photons would cause errors in the yield analysis.

By pumping the cavity at power levels much below the threshold value, the probability of generating more than one pair of photons is reduced. As noted in Chapter 2, our experimental setup had a roundtrip cavity loss of 3.3%, which was related to the cavity loss rate Γ and the free spectral range FSR by $2\Gamma/FSR$. We used a measurement time bin of duration T that could be varied in data analysis. Given a pump threshold of 300 mW and a desirable pump level of G^2=0.01, this suggested a pump power of ~3 mW for the doubly-resonant OPA. For our experiment, the pump power levels ranged between 100 μW and a few mW.

The coincidence counting procedure was as follows: When the fast and slow axes of the half-wave plate (HWP) were aligned accurately relative to the ordinary and extraordinary axes of the crystal, orthogonally-polarized signal and idler passed through the HWP without rotation. By rotating the HWP, the polarizations could be rotated by any desired angle. The amount of quantum interference that was expected between the signal and the idler depended on the HWP angle.

The number of coincidence counts was determined using a computer code written using the National Instruments LabView package. Data of 2 MB was acquired and downloaded from the GageScope memory to the computer after each 20-ms duration. It took approximately 6 seconds before data could be acquired again. Typically, we acquired data at a given setting for several hundred 20-ms periods. Unlike the usual coincidence-counting apparatus used in spontaneous downconversion experiments [6,7], which used a time-to-amplitude converter, we recorded the entire time trace and applied post-processing. This allowed us to vary the measurement time-bin interval T for the same set of data.

For a time bin of size T, a portion of each channel was scanned starting at every 10 ns position, and a coincidence was registered for the cases where there was a count in each channel within a time-bin duration T. Given that the data were taken with a resolution of 10 ns, the bin size T was a multiple of 10 ns. As shown in Figure 2-5, each photon registered as a 30-ns pulse at the GageScope. The output data from the GageScope was in the form of output voltages at 10 ns intervals for the data-acquisition duration of 20 ms. For no incident light on the detectors, the output voltage was ~0 V, whereas when a photon was registered, a positive voltage value of ~2.5 V was obtained. The post-

processing algorithm went through the record of voltage values in each channel and reduced the data to the "time-stamps" of the first value in time where a voltage above the threshold value (set within the program) was registered. For our purposes, the threshold was set to 2 V. Once the data in each channel were reduced to the time-stamps of the rise times, the software went through one of the channels (say, channel 1) and for each time stamp of channel 1, it looked for a time-stamp in channel 2 that was within a coincidence interval T relative to the time stamp of channel 1. (Note that using the time-stamps of the fall times, that is, the last value for which the voltage registered was greater than the threshold value, would have been an equally valid algorithm as long as the data in both channels were reduced in the same way.) The cases where there was exactly one rise-time stamp within a coincidence interval were registered as coincidences. The cases where there was more than one photon registered in one channel within T of a photon in the other channel were significantly fewer in number and they were discarded. The same set of data was processed for different coincidence intervals and the relation between the number of coincidences and the bin size was observed.

The different sets of data were acquired for different settings of the half-wave plate. In the experiment, the HWP and the PBS were set so that at $\theta = 0^\circ$ for the HWP, the horizontally polarized signal was transmitted while the vertically polarized idler was reflected. Figure 3-2 shows the coincidence counts over 250 20-ms durations for a total of 5 seconds of data for $\theta = 0^\circ$. The straight line corresponds to a minimum mean-squared error fit to the number of coincidences for different coincidence intervals. The linear fir for the intervals between 110 ns and 510 ns where the effects of cavity lifetime were not observed shows a coincidence intercept of 43.

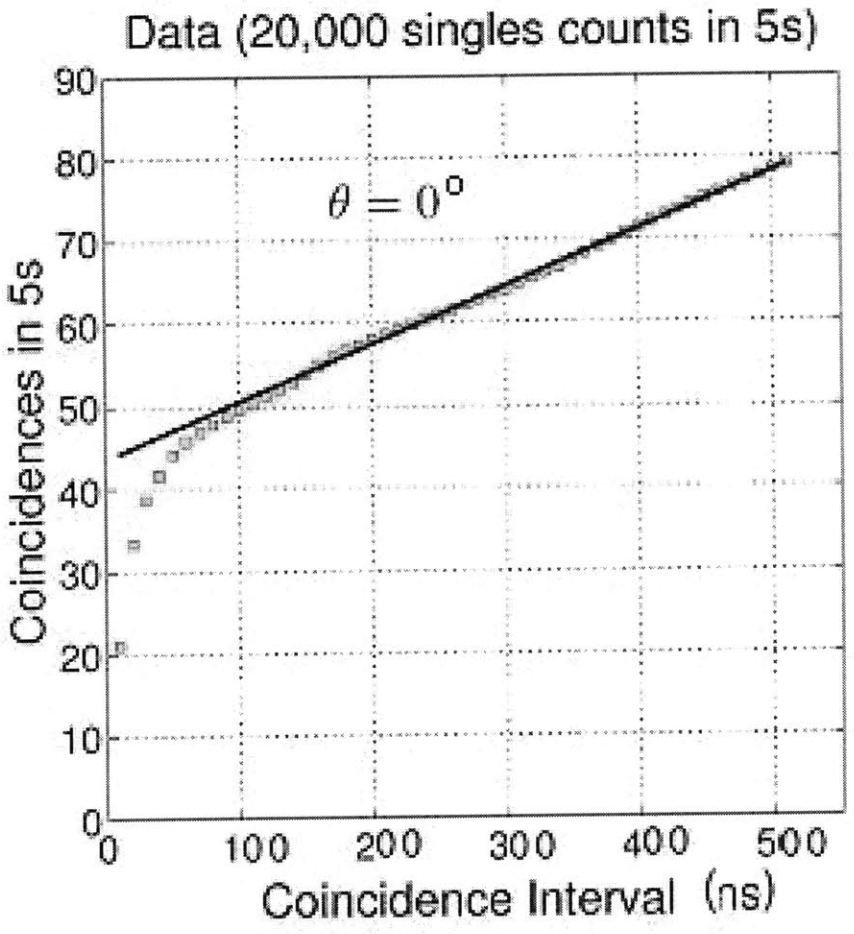

Figure 3-2 Coincidence counts at θ = 0° for different coincidence intervals T and a pump power of 100 μW. Coincidence intercept is 43.

For this set of data, the polarizations of the downconverted photons from the cavity were not rotated and the normally-ordered and phase-sensitive signal and idler correlation functions are given by

$$K^{(n)}(\tau)e^{i\omega_k\tau} \equiv \langle \hat{E}_k^{+}(t+\tau)\hat{E}_k(t)\rangle, \text{ for k = S, I} \tag{3.1}$$

$$K^{(p)}(\tau)e^{-i(\omega_p t+\omega_s\tau)} \equiv \left\langle \hat{E}_s(t+\tau)\hat{E}_I(t)\right\rangle \tag{3.2}$$

respectively [12]. The average singles rate at each detector is equal to the generation rate of signal (idler) photons within the crystal scaled by the quantum efficiency of the

detectors, η. The average singles counts for the signal and idler photons for an interval T are given by

$$\left\langle \hat{N}_S \right\rangle = \left\langle \hat{N}_I \right\rangle = \eta \int_0^T K^{(n)}(0)dt = \eta T K^{(n)}(0), \tag{3.3}$$

which, in terms of the cavity parameters can also be expressed as in (1.9). For time bins of duration T and measurement intervals of T_M, the expected number of singles at each detector is given by

$$S(T) = \frac{T_M}{T}\left\langle \hat{N}_S \right\rangle = \frac{T_M}{T}\left\langle \hat{N}_I \right\rangle = \eta T_M K^{(n)}(0). \tag{3.4}$$

The number of coincidences for the measurement intervals defined as in (3.4) is given by [12]

$$C(T) = \frac{T_M}{T}\left\langle \hat{N}_s \hat{N}_I \right\rangle, \tag{3.5}$$

where

$$\left\langle \hat{N}_S \hat{N}_I \right\rangle = \int_0^T dt \int_0^T du \left\langle \hat{E}_S^+(t)\hat{E}_S(t)\hat{E}_I^+(u)\hat{E}_I(u) \right\rangle . \tag{3.6}$$

Simplifying (3.5) by expanding (3.6), we get

$$C(T) = TT_M \left[\eta K^{(n)}(0)\right]^2 + \eta^2 T_M \int_{-T}^{T} d\tau \left(1 - \frac{|\tau|}{T}\right) \left|K^{(p)}(\tau)\right|^2 . \tag{3.7}$$

The first term in (3.7) corresponds to the "random" coincidences, that is the cases where each channel has a count within a time interval of T seconds, but these counts do not correspond to a pair of photons generated simultaneously within the bulk KTP crystal. The generation of random coincidences can be approximated by a Poissonian process with a given rate. The longer the period over which the counts are integrated, the more "random coincidences" we get. If the coincidences registered were purely

stochastic, we would expect to get a linear relationship between the number of coincidences and bin size that would go to zero coincidence for a bin size of zero. Figure 3-3 shows the experimental data acquired for the half-wave plate set at $\theta = 0°$ with an intercept of 43 and the contribution from the Poissonian term with an intercept of 0 (dashed line).

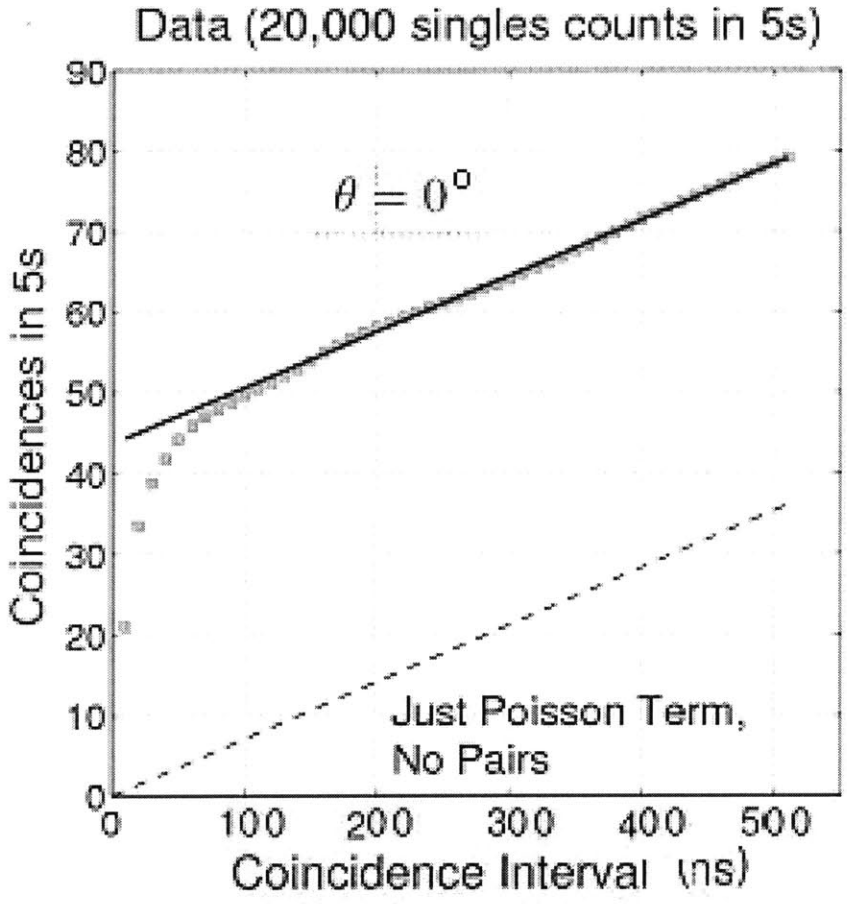

Figure 3-3: Plot of coincidences at $\theta = 0°$ (for a 100 μW pump power) and the Poissonian contribution. The dashed line shows the expected number of coincidences from random events.

The second term in (3.7) is the contribution from the signal-idler pairs. In the long-T limit, (3.7) reduces to

$$C(T) = TT_M\left[\eta K^{(n)}(0)\right]^2 + \eta^2 T_M \int_{-\infty}^{\infty} d\tau \left|K^{(p)}(\tau)\right|^2 . \tag{3.8}$$

The $T_M\left[\eta K^{(n)}(0)\right]^2$ term corresponds to the slope of the coincidence plots in Fig. 3-3 and the $\eta^2 T_M \int_{-\infty}^{\infty} d\tau \left|K^{(p)}(\tau)\right|^2$ term corresponds to the y-intercept of the line that is fitted to the coincidence data points. The singles rate is given by (3.4) and can be deduced graphically from the slope of the data shown in Figs. 3-2 and 3-3. The slope is approximately 37 / 0.5 μs = 74 x 10^6. From (3.4) and the coincidence slope $T_M\left[\eta K^{(n)}(0)\right]^2$, the singles generation rate S(T) is given by $\sqrt{(slope)T_M}$. For $T_M = 5$ seconds, we infer a singles count of ~ 19,000, which is in good agreement with the observed value of 20,000.

The number of coincidences exhibits a behavior that is approximately linear with the coincidence intervals except for relatively short intervals. This is due to timing jitter of the photons exiting the cavity. Since the OPA cavity had a 2.7% output coupler and the cavity lifetime was ~ 7 ns, the downconverted photons bounced around the cavity before exiting. Each of the pair of simultaneously-generated daughter photons could leave the cavity at different times. This introduced a substantial uncertainty between the arrival times of the two photons at their respective detectors, which were placed equidistant from the cavity. Hence, for short coincidence intervals we expect to see fewer coincidences because one photon could be detected while the conjugate photon could still be inside the cavity. Since the behavior for coincidence intervals longer than 100 ns exhibits an approximately linear behavior, as expected, a linear fitting was applied to the data points for coincidence intervals starting with 110 ns.

For the half-wave plate set at an angle 22.5° to rotate the downconverted photons by 45°, the set of coincidence data acquired is shown in Figure 3-4.

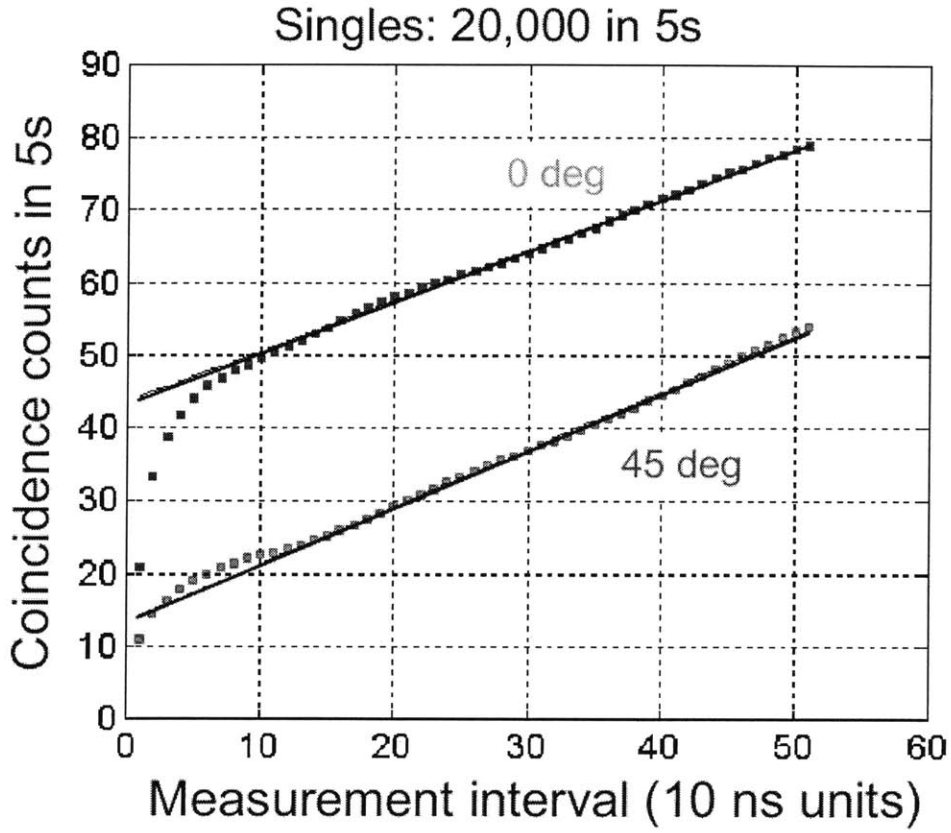

Figure 3-4 Plot of coincidences at $\theta = 0^\circ$ and $\theta = 45^\circ$ for a pump power of 100 μW.

By rotating the polarizations by 45°, each photon was equally likely to be reflected or transmitted at the polarizing beamsplitter in the experimental setup shown in Figure 2-7. Unlike the case $\theta = 0°$ in which the signal and idler were polarization-separated by the PBS, quantum interference might occur when the signal and idler had the same frequency and therefore were indistinguishable. The number of coincidences is once again given by (3.5), but this time the pairs term contains contributions due to quantum interference [12]

$$C(T) = TT_M\left[\eta K^{(n)}(0)\right]^2 + \eta^2 \frac{T_M}{2}\int_{-\infty}^{\infty} d\tau\left\{\left|K^{(p)}(\tau)\right|^2 - \mathrm{Re}\left[K^{(p)}(\tau)K^{(p)*}(-\tau)e^{-i(\omega_s-\omega_I)\tau}\right]\right\}. \quad (3.9)$$

The first term in (3.9) is the same as in (3.8) and as already mentioned, it is due to the Poisson terms. This also explains the identical slope of the two sets of data for $\theta = 0^\circ$ and $\theta = 45^\circ$. The lower number of coincidences observed for the set of data acquired for $\theta =$

45° is due to quantum interference which is given by the term $\mathrm{Re}\left[K^{(p)}(\tau)K^{(p)*}(-\tau)e^{-i(\omega_s-\omega_I)\tau}\right]$. The factor of ½ in front of the integral is the beamsplitter effect. For frequency nondegenerate pairs, the PBS acted as a 50/50 beamsplitter and hence statistically half of the time the photons would follow different paths, giving rise to a coincidence. For the other half of the time, both downconverted photons would follow the same path (either both being reflected or both being transmitted at the PBS), and hence there would not be a coincidence. Quantum entanglement requires a complete loss of distinguishability between the two daughter photons, which was sensitive to several factors such as frequency-degenerate operation, asymmetry of the correlation function ($K^{(p)}(\tau) \neq K^{(p)}(-\tau)$) and various spatial mode effects.

In the frequency-degenerate case, $\omega_s = \omega_I$, the quantum interference term, $\mathrm{Re}\left[K^{(p)}(\tau)K^{(p)*}(-\tau)e^{-i(\omega_s-\omega_I)\tau}\right]$ in (3.9) reduces to $\left|K^{(p)}(\tau)\right|^2$, if we assume a symmetric phase-sensitive correlation function. This results in the integral in (3.9) going to zero regardless of the measurement interval and the number of coincidences is given solely by the Poisson term $TT_M\left[\eta K^{(n)}(0)\right]^2$. Hence, if we had perfect degeneracy, the data for the case θ = 45° in Figure 3-3 would resemble the dashed-line in Figure 3-3 with an intercept of 0 and a slope given by $T_M\left[\eta K^{(n)}(0)\right]^2$. The fact that we have an intercept of 13 for the 45°-data implies that there was a nonzero contribution from the quantum interference term. If there was no quantum interference, Eq. (3.9) indicates that the coincidence intercept should be 21.5. If there had been complete entanglement, the coincidence rates for θ = 45° would have been down to the Poisson level. This suggests that we had partial quantum interference for the OPA outputs.

The second term in Eq. (3.8) corresponds to the coincidence intercept at T=0. The integral in (3.8) equals $K^{(n)}(0)$ and hence the intercept, $C_{int}(0) = \eta^2 T_M K^{(n)}(0)$. Since the singles rate is given by (3.4), we can easily determine the effective quantum efficiency of our experiment, η, by $\eta = C_{int}(0)/S(T)$. From our set of data, we get η=0.21%, which is significantly less than the intrinsic quantum efficiency of the SPDs determined using a highly-attenuated laser beam as described in Chapter 2. This indicates that there were additional losses in the propagation paths due to several factors including the cavity escape efficiency, angle walkoff, alignment and collection problems, and propagation and coating losses.

Taking the effective quantum efficiency of our experiment into account, we can see that for the set of data presented in Figs. 3-2 – 3-4 we have a production rate of ~ 1.8 x 10^6/s at 100 μW of pump. Over the phase-matching bandwidth of 320 GHz, the generation rate is ~5.6 x 10^4 pairs/sec/GHz/mW [12] in terms of pairs per second per GHz of bandwidth per mW of pump power. The broadband source described in [7] has a pair generation rate of 1.5 x 10^6/sec over a 3-THz bandwidth for a 150 mW pump power, corresponding to only 3 pairs/sec/GHz/mW.

Consider the singles counts as a function of the cavity mirror PZT sweep, as shown in Figure 3-5 and the expanded view in Figure 3-6. A National Instruments Counter/Timer Board (Model No. PCI-6602) and National Instruments Data Acquisition Kit for Windows were used in conjunction with LabView to display the real-time data from individual detectors.

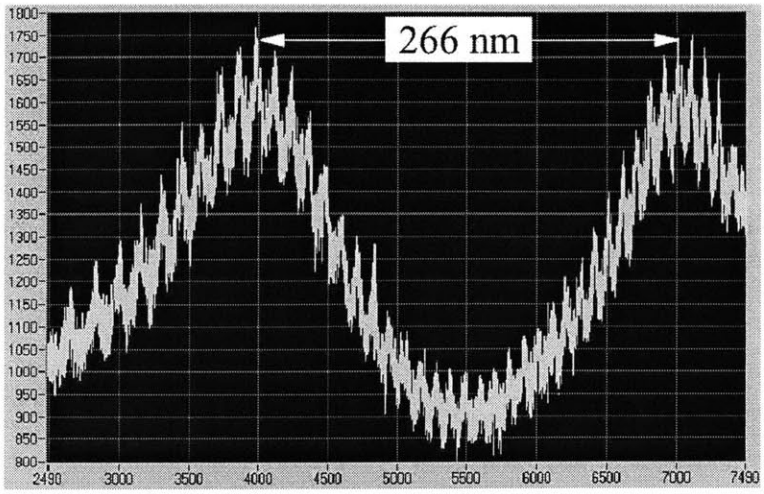

Figure 3-5 Singles count rate vs. cavity mirror PZT.

Figure 3-5 shows the presence of two resonances within the OPA cavity: One is the weak resonance of the pump at 532 nm, and the other is the signal-idler double resonance. The peak-to-peak cavity length change is 266 nm for the pump, and ~9.5 nm for the double resonance. Figure 3-6 shows some of these double resonance peaks on an expanded scale. It is well known that in a doubly-resonant optical parametric oscillator, the peak-to-peak separation is given by $(\Delta n\ FSR)/f_p$ [13]. For our OPA cavity, the double resonance peaks are estimated to be separated by 9.5 nm.

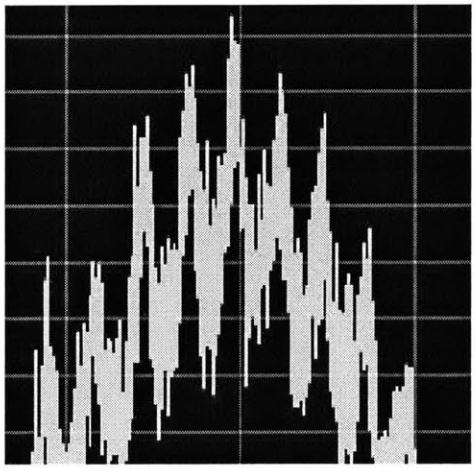

Figure 3-6 Expanded view of double-resonance peaks. The separation between the peaks is 9.5 nm.

Clearly, Fig. 3-5 indicates that in addition to the doubly-resonant signal-idler pairs, there was a large number of background counts. In fact, there should be three contributions to the output. First, there is the doubly-resonant narrowband component where both the signal and the idler were resonant with the cavity. The second component was the singly-resonant narrowband pair where only the signal or idler was resonant. The third is the nonresonant broadband component in which neither signal nor idler was resonant. The minima between the double resonance peaks in Fig. 3-6 represents the detected singles from nonresonant mode pairs (R_0) plus the singly-resonant pairs (R_1). The ratio of the doubly-resonant counts to the total counts is ~0.15. The simultaneous presence of these three components can best be explained graphically using figure 3-7.

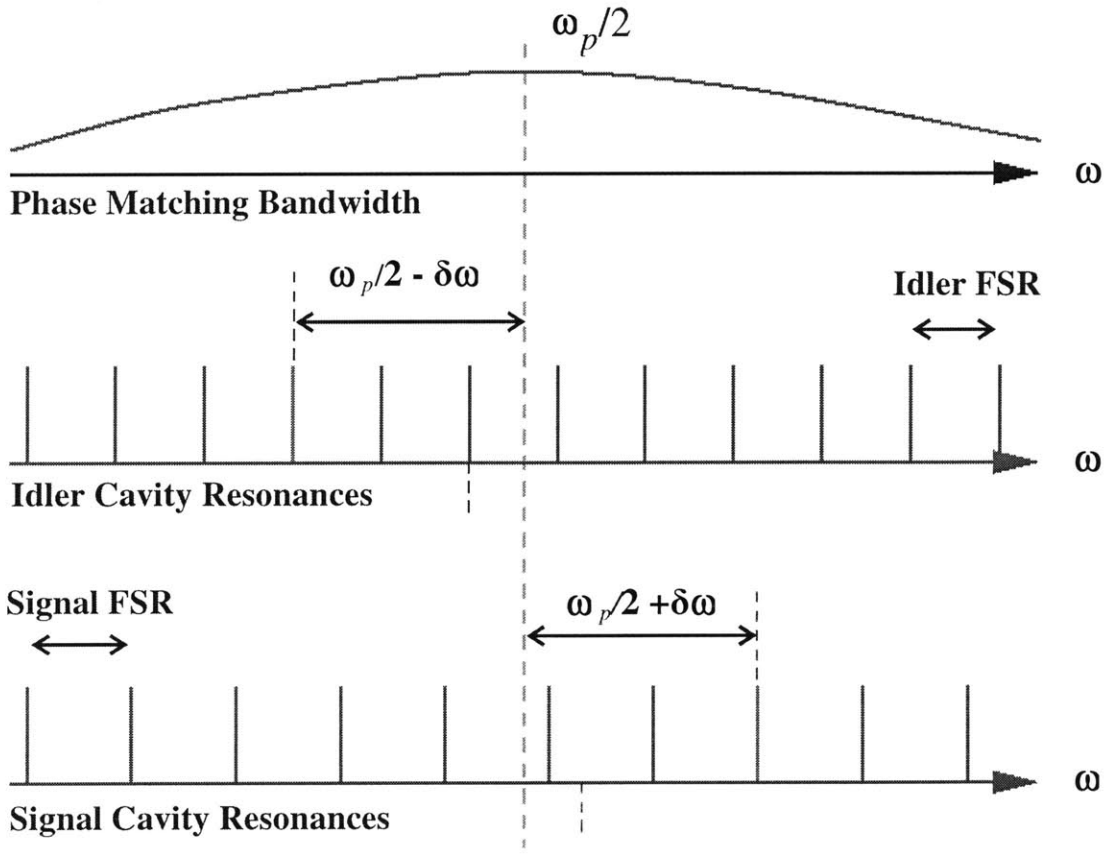

Figure 3-7 Cavity Resonances.

From the conservation of energy, the pump, signal and idler frequencies are related by

$$\omega_P = \omega_S + \omega_I \quad . \tag{3.10}$$

In the frequency-degenerate case, both the signal and the idler are at a frequency of $\omega_P/2$. However, in the more general case, if the idler is at a frequency $\omega_P/2 - \delta\omega$, the signal has to be at frequency $\omega_P/2 + \delta\omega$. The cavity imposes certain constraints on the resonant modes for the signal and idler. The daughter photons see different cavity lengths due to the different indices of refraction along the ordinary and extraordinary axes of the KTP crystal. Hence when the idler at frequency $\omega_P/2 - \delta\omega$ is resonant, there may not be any resonant signal field at frequency $\omega_P/2 + \delta\omega$, or vice versa, giving rise to a singly-resonant mode. When the pump photon downconverts into two daughter photons at frequencies where both the signal and the idler are resonant, the result is a doubly resonant mode.

For the OPA cavity used, the contribution of each one of these components to the singles rate can be calculated using the following equations [12]:

$$R_2 = G^2\Gamma \tag{3.11}$$

$$R_1 = 2R_2\left(\frac{(T+L)^2}{4T}\right)\frac{B_{SRO}}{B_{DRO}}\frac{B_{PM}}{FSR} \tag{3.12}$$

$$R_0 = R_2\left(\frac{(T+L)^2}{4T}\right)\frac{B_{PM}}{B_{DRO}}, \tag{3.13}$$

where R_2 is the contribution due to the singles count from the doubly-resonant component, R_1 from the singly-resonant component and R_0 from the nonresonant component. The output coupler transmission T was 2.7%, extra cavity losses L were

0.8%, pump level G^2 was ~1%. The singly resonant and doubly resonant bandwidths (B_{SRO} and B_{DRO}) were 30 MHz and 20 MHz respectively. The phase-matching bandwidth, B_{PM} of the cavity was 320 GHz and the free spectral range, FSR was 5.6 GHz. Γ is the cavity loss rate ($\Gamma/\pi = B_{SRO}$). Plugging in these numbers to Eqs. (3.11)-(3.13), and, for simplicity, adjusting G^2 such that R_2 = 1 x 10^6 pairs/s, we get 1.9 x 10^6 pairs/s from the singly-resonant components and 2.1 x 10^6 pairs/s from the nonresonant components. Hence, from these numbers, we estimate that only about 20% of the photons were generated at the doubly-resonant frequencies. This is close to the observation value of 15% in Figs. 3-5 and 3-6.

The ratio of the coincidence intercepts indicates the presence of quantum interference as already mentioned,

$$r = \frac{C_{\text{int}}(0)\,|_{\theta=45^o}}{C_{\text{int}}(0)\,|_{\theta=0^o}} = \frac{13}{43} = 0.30 \tag{3.14}$$

If we suppose that the nonresonant pairs give perfect quantum interference and the other components give none, the intercept ratio should be given by

$$r = \frac{(R_1 + R_2)/2}{R_0 + R_1 + R_2} \tag{3.15}$$

For the values of R_0, R_1 and R_2 above, we get r = 0.29 indicating that this assumption agrees with what we actually observed in the experiment. However, it is likely that the cavity was not tuned to the peak of double resonance. This would mean R_2 = 0 and would give a coincidence ratio, r, of 0.24. This implies that we should have fewer coincidences than we observed. The most likely case is that we had some doubly-resonant mode pairs and the quantum interference due to the nonresonant mode pairs was not complete.

In order to generate triplet states by beamsplitting the output from the OPA, we need to operate at frequency degeneracy. Since the singly-resonant and doubly-resonant components were narrowband, tuning them to frequency degeneracy was hard, and no effort was made to achieve degeneracy for these components. However, the significantly broader bandwidth of the nonresonant mode pairs made it possible to tune these components to frequency degeneracy. A nonresonant mode pair with individual photons at frequencies $\omega_{\pm} = \omega_P/2 \pm \delta\omega$ is in the triplet state [12]

$$|\Psi\rangle_{SI} \equiv \left(|\uparrow\rangle_{\omega_+} |\bullet\rangle_{\omega_-} + |\bullet\rangle_{\omega_+} |\uparrow\rangle_{\omega_-} \right) / \sqrt{2} \quad , \tag{3.16}$$

where the arrow and the dot represent vertical and horizontal polarizations, respectively, and $\delta\omega << B_{PM}$. After the polarization rotation of 45°, the state becomes

$$|\Psi'\rangle_{SI} \equiv \left(|\uparrow\rangle_{\omega_+} |\uparrow\rangle_{\omega_-} + |\bullet\rangle_{\omega_+} |\bullet\rangle_{\omega_-} \right) / \sqrt{2} \quad . \tag{3.17}$$

When $|\Psi'\rangle_{SI}$ encounters the PBS, both of the photons in the pair take the same path. Although they are equally likely to take either path, since they always take the same path, the number of coincidences is reduced. This only occurs for frequency-degenerate pairs as can be seen from (3.9). When $\omega_S = \omega_I$, the number of coincidences is significantly reduced (and goes to zero for symmetric phase-sensitive correlation term $K^{(p)}(\tau)$) as already discussed. After the 45° rotation, the PBS acts as a 50/50 beamsplitter for the frequency-nondegenerate pairs, resulting in distinguishable signal-idler photon pairs [12]. There is a 50% chance that those pairs end up in different detectors and therefore the number of coincidences that would be expected if all the photon pairs were nondegenerate would be half the number for the case with no polarization rotation (HWP

set at 0°). The fact that the ratio of the coincidences for the 0° and 45° cases is not 0.5 tells us that we have generated polarization-entangled triplets in our experiment.

Chapter 4

Conclusion: Summary and Future Work

In this thesis we have achieved preliminary results demonstrating a cw ultrabright source of downconverted photons using a KTP optical parametric amplifier. We generated photon pairs at a rate of 5.6 x 10^4 pairs/sec/GHz/mW, which is significantly brighter than the previous sources with only 3 pairs/sec/GHz/mW [7]. Despite the low quantum efficiency at the wavelength of operation, we have successfully used a KTP doubly-resonant OPA to demonstrate and characterize cavity-enhanced downconversion.

We have shown that there were three contributions to the downconverted photons in a doubly-resonant optical parametric amplifier – the narrowband doubly resonant, narrowband singly resonant and broadband nonresonant components. The singly resonant contribution was about twice as large as the doubly resonant contribution. We have also demonstrated that the frequency degenerate nonresonant mode pairs were polarization-entangled triplets and quantum interference due to these triplets was observed. We can infer that the generation rate for these broadband polarization-entangled triplets is 7 x 10^6 /sec/mW over a 320 GHz bandwidth [12].

Future experiments employing an intracavity polarizing beamsplitter to form a singly-resonant cavity can be built to utilize the singly-resonant component. Based on the generation rates R_0 and R_1 and the number of singly-resonant modes, we can infer that the singly-resonant pairs would have a generation rate of 6 x 10^4 pairs/s over a 30-MHz

bandwidth [12]. This would give us a viable method for obtaining narrowband entangled photons.

We have also shown that using a bulk KTP crystal rather than beta barium borate (BBO) which is generally used, the production efficiency of downconversion is much higher. The length of the crystal used, collinear propagation within the crystal and the high nonlinear coefficient of KTP have contributed to the higher efficiency.

Our results will help guide future experiments that utilize cavity-enhanced downconversion. For example, an ongoing experiment uses a periodically poled KTP crystal with a UV pump at 397 nm and outputs at 795 nm. The 795 nm wavelength matches the atomic transition of Rb for quantum memory applications. A significant difference between the KTP and the PPKTP experiments is the higher (~50 %) quantum efficiency of the detectors at the output wavelengths for the PPKTP and hence results that enable more in-depth analyses can be expected.

Bibliography

[1] Bennett C H and Shor P W 1998 *IEEE Trans. Inf. Theory* **44** 2724

[2] Ekert A K 1991 *Phys. Rev. Lett.* **67** 661

[3] Bennett C H, Brassard G, Crépeau C, Josza R, Peres A and Wootters W K 1993 *Phys. Rev. Lett.* **70** 1895

[4] Shapiro J H, "Long-distance high-fidelity teleportation using singlet states" *quant-Phy* / 0105055

[5] Lloyd S, Shahriar M S, Hemmer P R, "Teleportation and the quantum internet", submitted to *Phys. Rev. A (quant-phy / 003147)*

[6] Kwiat P G, Mattle K, Weinfurter H, Zeilinger A, Sergienko A V, Shih Y 1995 *Phys. Rev. Lett.* **75** 4337

[7] Kwiat P G, Waks E, White A G, Appelbaum I, Eberhard P H 1999 *Phys Rev. A* **60** R773

[8] Shapiro J H, Wong N C 2000 *J. Opt. B: Quantum Semiclass. Opt.* **2** L1

[9] Teja J, Wong N C 1998 *Optics Express* **2** 65

[10] Kogelnik H, Li T 1966 *Applied Optics* **5** 1550

[11] Haus H A *Waves and Fields in Optical Electronics*. Prentice-Hall, New Jersey, 1984

[12] Kuklewicz C E, Keskiner E, Shapiro J H, Wong N C "A high-flux entanglement source based on a doubly resonant optical parametric amplifier", presented at the *7th International Conference on Squeezed States and Uncertainty Relations,* Boston, MA. June 2001.

[13] Lee D, Wong NC 1993 *Journal of the Optical Society of America B-Optical Physics* **10** 1659.